Experimental investigations and kinematic simulation of single grit scratched surfaces considering pile-up behaviour: grinding perspective

Dinesh Setti*, Benjamin Kirsch, Jan C. Aurich
Institute for manufacturing technology and production systems (FBK)
Technical University Kaiserslautern, Rhineland-Palatinate, Germany
*corresponding author: dinesh.setti@mv.uni-kl.de

Abstract: Scratch tests are useful techniques to gain insight into the material removal mechanism of abrasive machining processes. In most of the scratch tests, uncut chip thickness value is either constant or vary from zero to maximum. However, in abrasive machining processes, uncut chip thickness value ranges from either zero to maximum or vice-versa. Moreover, regular scratch tests conducted at very low speeds, and in which either the indenter or the workpiece is stationary. Because of these limitations, the knowledge obtained from the existing scratch test results is not valid for most of the abrasive processes. Hence, in this paper, the influence of chip thickness variation, speed ratio, and depth of cut on the pile-up behaviour of AISI 1015 steel and 2017A-T4 aluminium alloy surfaces were investigated. The workpiece having the comparable thermal diffusivity value with the grit has shown a significant difference in its pile-up behaviour. Through a better understanding of chip thickness influence on pile-up ratio, a mathematical was developed for kinematic simulations. Using the developed model, kinematic simulations were done to visualise the scratch surface topography and material pile-up by considering the grit trajectory path and chip thickness variation. Finally, simulated surfaces were compared with the experimental results to show the proposed method applicability.

Keywords: kinematic simulations, scratching, surface grinding, minimum chip thickness, single grit, ploughing, pile-up.

Nomenclature:

a_p	programmed or set depth of cut	µm
b	width of the scratch	µm
b_p	pile-up width	µm
b_{pl}	left side pile-up width	µm
b_{pr}	right side pile-up width	µm
b_{pt}	pile-up width at ploughing to cutting transition position	µm
b_t	width of the scratch at ploughing to cutting transition position	µm
c_p	specific heat capacity	J/kg·K
d	depth of the groove	µm
d_c	critical depth of cut	µm
h_p	pile-up height	µm
h_{pl}	left side pile-up height	µm
h_{pr}	right side pile-up height	µm

h_{pt}	pile-up height at ploughing to cutting transition position	µm
h_{cu}	uncut chip thickness	µm
$h_{cu\ max}$	maximum uncut chip thickness	µm
h'	minimum chip thickness	µm
h'_{entry}	entry region minimum chip thickness	µm
h'_{exit}	exit region minimum chip thickness	µm
h'_{total}	minimum chip thickness considering entry and exit regions together	µm
h_s'	static minimum chip thickness	µm
h_d'	dynamic minimum chip thickness	µm
k	thermal conductivity	W/m·K
l_c	contact length	mm
l_g	geometric contact length	mm
l_k	kinematic contact length	mm
q	speed ratio (v_c/v_w)	-
v_c	cutting speed	m/s
v_w	work speed	m/min
x, y, z	position coordinates	-
A_1, A_2	cross-sectional area of pile up material	µm^2
A_3	cross-sectional area of the groove	µm^2
D	diameter of the wheel	mm
E	Young's modulus	GPa
E^*	equivalent Young's modulus	GPa
Y	yield strength	MPa
r_o	cutting edge radius	µm
r_e	nose radius	µm
ρ	density	kg/m^3
α	thermal diffusivity ($k/\ \rho.c_p$)	m^2/s
ϑ	Poisson's ratio	-

Introduction:

Abrasive processes are widely used to produce components with the high surface finish and dimensional accuracy for electronics, optics, and aerospace applications usually made out of hard, and difficult to machine materials [1]. Despite this fact, the majority of the operations in the industry are still conducted according to the thumb rules based on the workers experience due to the lack of predictive models that deal with surface integrity [2]. To a large extent, it can be attributed to the abrasive processes complexity compared to the machining operations with well-defined tool geometries such as turning, milling, and drilling. Different methods such as fuzzy logic, artificial neural networks, and regression modeling are available to predict the process responses in terms of known variables. Simulation techniques such as finite element (FE), kinematic and molecular dynamics (MD) are developed to visualise the responses in a given 2D or 3D space [3]. Because

of better understanding and visualisation, simulations are getting more extensive attention, although a valid model is required to perform the simulations. MD simulation helps to understand the process at the microscopic level and especially useful to study the phenomenon covering gases, liquids, and solids [4]. FE simulation helps to explore the process at both micro and macroscopic levels. Most of the FE simulation work at the macroscopic level were confined to the thermal analysis, and works at the microscopic level were limited to the single grit interactions rather than the whole process due to the higher computational times [5,6]. In a shorter time, kinematic simulations can give a 3D view of the finished surface based on ideal geometric penetration of abrasive grits into the workpiece compared to the FE and MD simulations [7]. Majority of the 3D geometric-kinematic models were developed for grinding process by considering several aspects of the process such as: machine process interactions [8], vibrations [9,10], wheel wear [11], different grit shapes [12–14], and dressing effect [15]. In recent years, progress has been made on predicting the ground surface topography by virtual wheels modelled based on the stochastic analysis of grinding wheel topography measurements [16–20]. However, the applicability of the kinematic simulation primarily depends upon the integration of accurate material removal mechanism.

Scratch tests are useful techniques to understand the material removal mechanism of individual abrasive grits. These scratch tests classified mainly as rotating and linear type. In rotating scratch tests (figure 1a), the abrasive grit passes over the work surface, and its uncut chip thickness value varies from zero to a maximum value (a_p or $h_{cu\ max}$) and then reaches to zero at the end of the cut. In linear scratch tests, abrasive grit moves over the work surface either with a constant ($h_{cu\ max}$) or gradually increased uncut chip thickness value (0 to $h_{cu\ max}$) (figure 1b and 1c). Irrespective of the test nature, at the beginning of the scratch, grit makes elastic contact with the workpiece, which does not contribute to the material removal, followed by the ploughing and chip formation. On an average, chip formation commences only after attaining a certain depth of cut, also known as critical depth of cut (d_c) or minimum chip thickness ($h^{\prime}$) value.

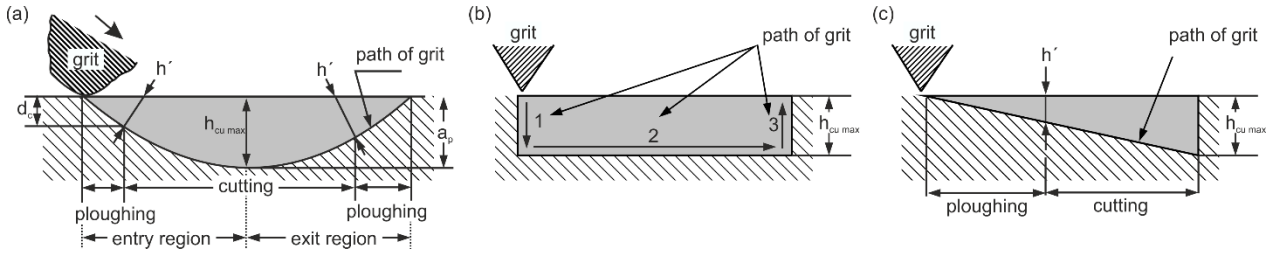

Figure 1. Illustration of uncut chip thickness variation along the grit path in (a) rotating scratch test, (b) linear scratch test with a constant uncut chip thickness value, (c) linear scratch test with the gradual increased uncut chip thickness value

Factors that can affect the critical depth of cut value include the geometry of grit, its orientation, its rake angle, and the friction coefficient [21]. Even after chip formation starts, ploughing still exists, as some of the material from the cutting path pushed aside into ridges. From the linear scratch tests with different indenters, a rake angle was found, where the chip formation starts after the ploughing phase and called a critical rake

angle [22,23]. However, linear scratch tests could transfer very little information to the grinding process because of the grit trajectory path. Moreover, experiments similar to the grinding (rotating single grit scratching, fly milling) revealed the depth controlled transition from ploughing to cutting and referred the corresponding uncut chip thickness value as minimum chip thickness, which accounted for the well-known size effect in grinding [24] as well as in micro machining processes [25].

There are predominantly two methods available to evaluate the minimum chip thickness value considering the scratch surface profile for the ductile materials. The first method (Figure 2) considers the variation between the groove area and pileup area, and the second method considers the variation between groove depth and scratch length.

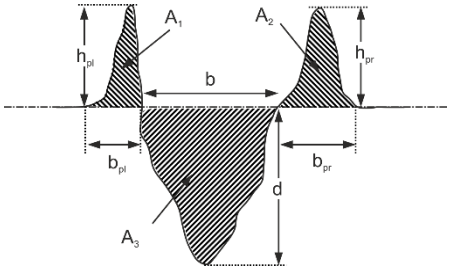

Figure 2. A typical transverse trace of a scratch at a specific groove depth

Out of these two methods, the first method is preferred due to the accuracy and its independent nature on the scratch starting position. In this method, the pile-up ratio is used to identify the different regimes such as rubbing, ploughing, and cutting. Pile-up ratio is the ratio between cross-sectional areas of pile-up and groove.

$$Pile-up\ ratio = \frac{(A_1+A_2)}{A_3} \quad (1)$$

According to the pile-up ratio, different regimes classified as given below [26].

rubbing region	:	$A_1 = A_2 = A_3 = 0$	pile-up ratio	:	$\approx \infty$
ploughing region	:	$(A_1 + A_2) > A_3$	pile-up ratio	:	> 1
transition region	:	$(A_1 + A_2) \approx A_3 \neq 0$	pile-up ratio	:	≈ 1
cutting region	:	$(A_1 + A_2) < A_3$	pile-up ratio	:	< 1

From the literature, it can be observed that the reported works on the rotating scratch tests with various relative moments between the grit and work surface are few as summarised in Table 1.

Table 1 Summary of the available scratch test literature classified according to grit and workpiece kinematics

author	grit and workpiece materials	grit kinematics (stationary/rotating/linear)	workpiece kinematics (stationary/moving)
Graham [23]	tungsten carbide (grit)/ Al-alloy(workpiece)	rotating (2.83 m/s)	stationary

Buttery and Hamed [27]	Rockwell, Vickers indenters/ SKF ball bearing steel, mild steel, duralumin alloy	linear (up to 37 m/s)	moving (17.7 m/min)
Buttery and Hamed [28]	Rockwell, Vickers indenters/ SKF ball bearing steel with different heat treatments	linear (up to 20 m/s)	moving (17.7 m/min)
Kita et al., [29]	cemented carbide, diamond/ carbon steel	rotating (up to 33 m/s)	stationary
Moneim et al., [22]	HSS/ free machining brass	linear (0.013 m/s)	stationary
Matsuo et al., [30]	cBN and diamond / SUJ2, S50C, SS41 steels, and alumina	rotating (14, 30 m/s)	stationary
Ohbuchi and Matsuo [31]	cBN and diamond/ S50C steel	rotating (10, 20 m/s)	moving (0.33 m/s)
Wang et al., [32]	diamond / pure titanium	rotating (1-4 m/s)	stationary
Klocke et al., [33]	sintered corundum/ C45E steel	linear (45 m/s)	moving (180 mm/min)
Subhash and Zhang [34]	diamond/ steel	rotating (105 m/s)	stationary
Brinksmaier and Glwerzew [35]	synthetic diamond/ case hardened steel 1.7131	rotating (0.3-3.1 m/s)	moving (300 mm/min)
Barge et al., [36]	tungsten carbide/ AISI4142 steel	rotating (52 m/s)	moving (0.5 mm/min)
Ghosh et al., [37]	diamond/ aluminium	stationary	rotating (16.7 m/s)
Aurich and Steffes [38]	cBN/ heat treated steel AISI 4140H	rotating (60-120 m/s)	moving
Anderson et al., [39]	diamond/ AISI4340	rotating (5-30 m/s)	moving (180 mm/min)
Öpöz and Chen [40]	cBN / En24T steel, Inconel 718	rotating (5-10 m/s)	stationary
Dai et al., [41]	diamond/Inconel 718	rotating (30-160 m/s)	moving (97-547 mm/min)
Tian et al., [42]	diamond/ GH4169 superalloy	rotating (20-165 m/s)	moving (perpendicular to cutting speed direction)

It is evident from the table 1 that the experiments have been conducted on very ductile materials such as aluminium and brass also to understand the material removal mechanism and to compare with the other materials irrespective of their grinding application. Moreover, all the works mentioned in Table 1 confirmed the influence of kinematic conditions on cutting behaviour.

In rotating scratch tests, a scratch made by the single grit consists of two regions such as entry and exit region as shown in figure 1a. Theoretically, the variation of uncut chip thickness geometry in the entry and exit region represents the up and down grinding respectively, despite the same velocity directions. Owing to this,

in up and down modes, process responses such as forces and temperature profile varies irrespective of the geometrical symmetry [43]. From table 1, it can also be observed that most of the works associated with the single grit scratch tests considered either the workpiece or the grit as a stationary object. A few works considered both as the moving objects either at a fixed low-speed ratio or at the very high-speed ratio. All these cases failed to show the influence of relative speed between the grit and workpiece on the material removal mechanism in conventional surface grinding conditions, i.e., the speed ratio is in between 100-200 [21]. The relative speed between wheel and work surface determines the heat source moving rate that influences the thermal effects inside the workpiece [44]. Hence, thermal softening and strain hardening phenomenon also vary, which in turn may affect the minimum chip thickness value. Therefore, in the present work, the interaction between the grit and the workpiece is studied to provide an insight into the effect of kinematic condition and chip thickness variation on the material deformation mode. As the experimental conditions also play a significant role, investigations were conducted under possible high-speed ratios. Further, based on the experimental observations, a methodology has been developed to model the pile-up height and to simulate the scratch surfaces considering separate minimum chip thickness values for the entry and exit regions.

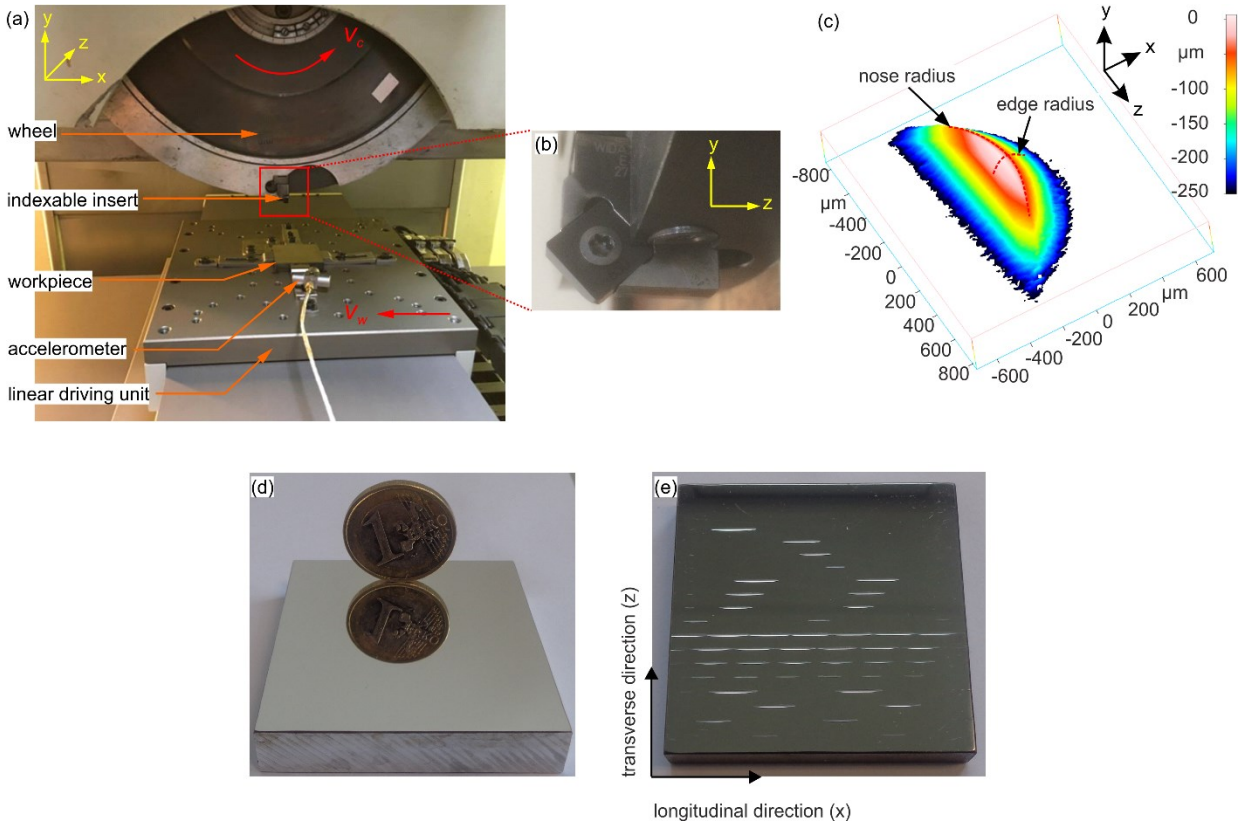

Figure 3. (a) experimental setup for rotating single grit scratch tests (b) close view of the utilized indexable insert (c) 3D view of the cutting edge (d) mirror polished workpiece surface before experiments (e) scratches on the work surface after experiments

Experimental method:

Rotating single grit scratch experiments were performed on a high performance-grinding machine (ELB CAM MASTER I/1 FR)[1]. A customised wheel (diameter 400 mm) with an indexable insert was used as a grinding wheel. The experimental setup is shown in figure 3a. As the available grinding machine was not able to provide the high table speeds, an additional linear driving unit was utilised to achieve the required feed rates.
A ceramic insert (Si_3N_4) (Figure 3b)was used as the abrasive grit for the present experiments due to the well-defined geometry similar to Barge et al., [36]. Due to the known geometry (Figure 3c), using an indexable insert as the abrasive grit helps analyse the results and in the case of fracture during the experiments, it can be replaced with the similar one. The indexable insert has a nose and cutting-edge radius of approximately 794 µm and 15 µm respectively. Here onwards, in this work, the indexable insert referred to as the grit. Two work materials AISI 1015 steel and 2017A-T4 aluminium alloy were selected to ensure a vast difference in their equivalent Young's modulus to yield strength ratio (E*/Y). Higher the E*/Y ratio, lower the expected minimum chip thickness and vice-versa [45]. Equivalent Young's modulus can be calculated with the following expression.

$$\frac{1}{E^*} = \frac{(1-\vartheta_1^2)}{E_1} + \frac{(1-\vartheta_2^2)}{E_2} \qquad (2)$$

Mechanical properties of the selected grit and work materials are given in Table 2. It also includes the thermal properties of commonly employed abrasive materials for comparison. Given E*/Y values for work material was calculated with to Si_3N_4 grit.

Table 2. Properties of grit and work materials [46,47]

	E (GPa)	Y (MPa)	ϑ	k (W/m.K)	$\times 10^3$ ρ (Kg/m^3)	α (mm^2/s)	c_p (J/Kg.K)	E^*/Y	h'/r_o [45]
AISI 1015 steel	200	325	0.29	51.9	7.87	14.03	470	406.45	0.1437
2017A-T4 alloy	72.4	276	0.33	134	2.79	54.5	880	236.83	0.2832
Si_3N_4	310	-	0.27	30	3.29	13.81	660	-	-
diamond	-	-	-	600-2000	3.52	333-1110	511	-	-
cBN	-	-	-	240-1300	3.48	136-738	506	-	-
SiC	-	-	-	100	3.21	44	710	-	-
Al_2O_3	-	-	-	35	3.98	11.5	765	-	-

Sample surfaces were prepared by polishing and ensured to have an average roughness (S_a) value of less than 0.1 µm before the scratching process (see Fig. 3d). After placing the workpiece on the linear driving unit, a dial gauge was used to verify the flatness. Errors were minimized by levelling the workpiece with the help of very

[1] Naming of specific manufacturers is done solely for the sake of completeness and does not necessarily imply an endorsement of the named companies nor that the products are necessarily the best for the purpose.

thin metal strips, which were placed below the work surface. Experimental conditions were selected within the typical range of surface grinding conditions (maximum table speed 15 m/min and a minimum cutting speed of 5 m/s). The workpiece needs to travel a specific distance in the longitudinal direction to avoid overlapping of scratches. Hence, to meet this requirement, minimum possible table speed and maximum possible cutting speeds were identified. To check the scratches interaction, scratches were made on the work surface with different speed (initial maximum cutting speed value is 60 m/s, and initial minimum table speed value is 1 m/min) combinations at 40 μm depth of cut. These values were gradually varied, and where no interaction between the individual scratches was observed, those (table speed 5 m/min and cutting speed 30 m/s) values were selected for the further experiments. Each experiment was repeated thrice to ensure the accuracy of the reported results. Table 3 gives the detailed experimental conditions, as mentioned earlier, the maximum possible depth of cut and maximum speed ratio values were considered to ensure the temperature influence on scratching unlike standard scratch tests with micro and nano-indenters.

Table 3. Summary of the experimental conditions

No.	q	a_p (μm)	v_w (m/min)	v_c (m/s)
1	20	10	15	5
2	20	20	15	5
3	20	30	15	5
4	20	40	15	5
5	60	10	5	5
6	60	20	5	5
7	60	30	5	5
8	60	40	5	5
9	120	10	15	30
10	120	20	15	30
11	120	30	15	30
12	120	40	15	30
13	360	10	5	30
14	360	20	5	30
15	360	30	5	30
16	360	40	5	30

All the experiments were performed in the longitudinal direction to create identical scratches (Fig 3e). During the longitudinal scratching, the wheel was rotated, and the workpiece was moved in the opposite direction. The depth of cut was set by adjusting the wheel in Y-axis. The single grit wheel was moved down slowly until it makes initial contact with the workpiece surface. To ensure precise contact, this process was monitored by the accelerometer (Kistler, 8692C50) signals. At the initial contact position, the coordinate value in the Y-axis

was considered as zero, and the workpiece was moved away in X-axis direction. The depth of cut and the wheel rpm related to the required cutting speed were adjusted, and the linear driving unit was moved with the required feed rate to make the scratches. After one pass, the process was repeated by shifting the table in the Z-axis direction to generate the scratches for another set of conditions. After all the experiments, transverse sections of scratches were analysed with an optical 3D measuring instrument GFM MikroCAD supported with ODSCAD software. This instrument has a lateral and vertical resolution, and the measurement range of 0.7 µm, 0.07 µm, and 500 µm respectively. Each scratch was inspected at 12 distinct positions in between the starting and end points (first six measurements correspond to entry region, and last six corresponds exit region) to measure the pile-up area, groove area, and groove depth as shown in Figure 4a. In Figure 4b, for the same condition, the microscopic image for the entry and exit regions is given.

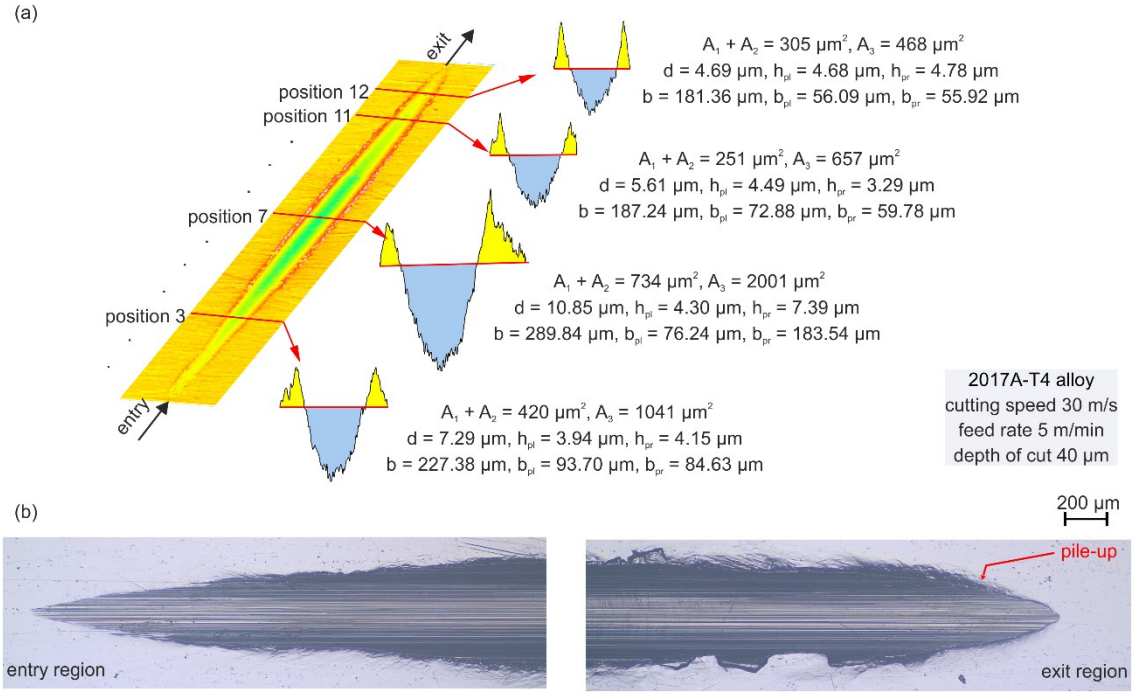

Figure 4. (a) Cross-sectional profiles of a single scratch at various positions along the scratch length direction (b) microscopic image of the scratch in entry and exit regions

Results and Discussions:

For every experimental condition, the relation between the pile-up ratio and groove depth was identified by fitting the most suitable power fit curve to find the minimum chip thickness value as shown in Figure 5. Because, by measurements, it was difficult to identify the exact transition position between the ploughing to cutting. It is also difficult to distinguish the pile-up and the background workpiece surface texture, especially at the entry side.

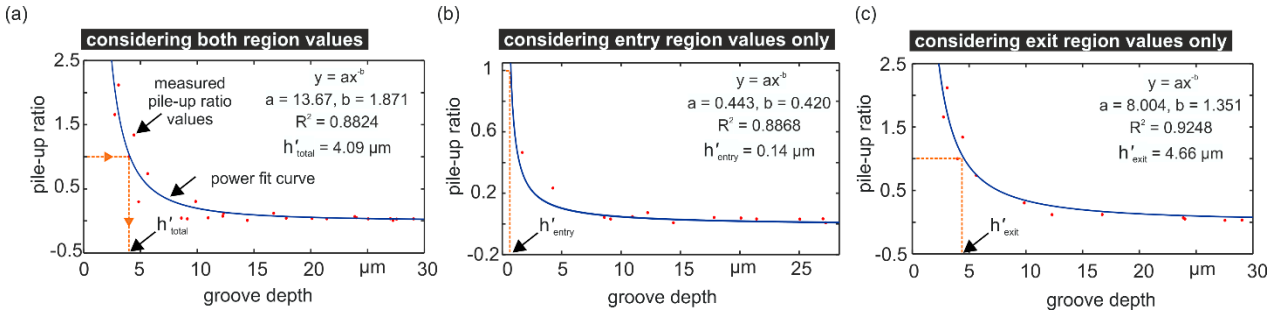

Figure 5. Example of minimum chip thickness values identification based on the pile-up ratio values (a) considering both region values together for the analysis, (c) considering the entry region values only, and (c) considering the exit region values only (speed ratio 360, depth of cut 30 µm, AISI 1015 steel)

Measurements outside the 95% confidence bounds of the power fit curve were deleted as outliers. The groove depth value (x-axis), at which pile-up ratio (y-axis) is equal to one was calculated using the model constants (a and b, indicated in Figure 5) and considered that depth value as minimum chip thickness value. The coefficient of determination (R^2) value indicates the goodness of curve fitting. From Figure 5, the difference in the minimum chip thickness value is evident in each region. It is an expected behaviour due to the material accumulation, and interference of the strain rate and temperature [48] as explained by several researchers [26,36]. Hence, to represent a realistic situation, each region values were considered individually (like Figure 5b and 5c) and compared with the evaluations based on both region values (like Figure 5a). Summary of the obtained minimum chip thickness values for all the conditions is given in Table 4**Error! Reference source not found.**.

Table 4 Summary of the measured minimum chip thickness values

S. No	a_p (µm)	q	h' (µm)						percentage of error compared to h_s'					
			2017A-T4 alloy			AISI 1015 steel			2017A-T4 alloy (h_s' = 4 µm [45])			AISI 1015 steel (h_s' = 1.75 µm [45])		
			h'_{entry}	h'_{exit}	h'_{total}	h'_{entry}	h'_{exit}	h'_{total}	h'_{entry}	h'_{exit}	h'_{total}	h'_{entry}	h'_{exit}	h'_{total}
1	10	20	3.90	4.86	4.66	2.00	3.99	3.98	-2.6	21.6	16.5	14.2	128.1	127.4
2	20	20	4.91	6.90	4.44	1.23	5.54	5.00	22.7	72.5	11.0	-30.0	216.6	185.7
3	30	20	6.10	7.92	4.54	0.98	6.00	6.17	52.5	97.9	13.5	-43.8	242.8	252.6
4	40	20	6.84	8.48	5.40	0.69	7.58	7.24	71.1	112.0	35.0	-60.6	333.1	313.7
5	10	60	3.64	4.33	3.14	1.59	3.27	3.58	-9.0	8.3	-21.5	-9.0	86.8	104.6
6	20	60	4.16	6.04	4.51	0.91	4.33	4.80	4.1	50.9	12.8	-47.9	147.5	174.3
7	30	60	4.45	6.21	4.48	0.64	4.89	5.54	11.3	55.3	12.0	-63.6	179.2	216.6
8	40	60	5.59	7.02	4.84	0.62	7.50	6.60	39.7	75.6	21.0	-64.3	328.5	277.1
9	10	120	3.86	3.79	4.25	1.60	3.59	3.01	-3.5	-5.2	6.3	-8.6	105.0	72.0
10	20	120	3.96	4.11	3.86	0.71	4.97	4.55	-1.1	2.6	-3.5	-59.6	184.2	160.0

11	30	120	4.16	5.07	4.36	0.39	4.77	4.92	4.0	26.8	9.0	-77.6	172.6	181.1
12	40	120	4.77	5.44	4.68	0.03	6.58	5.76	19.4	36.0	17.0	-98.6	276.3	229.1
13	10	360	3.92	3.81	3.44	1.16	3.59	1.81	-2.0	-4.7	-14.0	-33.8	105.4	3.4
14	20	360	3.81	3.71	3.27	0.42	4.10	2.66	-4.8	-7.3	-18.3	-76.2	134.3	52.0
15	30	360	3.79	3.48	3.16	0.14	4.66	4.09	-5.3	-13.0	-21.0	-91.8	166.3	133.7
16	40	360	3.72	3.52	2.63	0.00	5.68	4.93	-7.0	-11.9	-34.3	-99.7	224.6	181.7

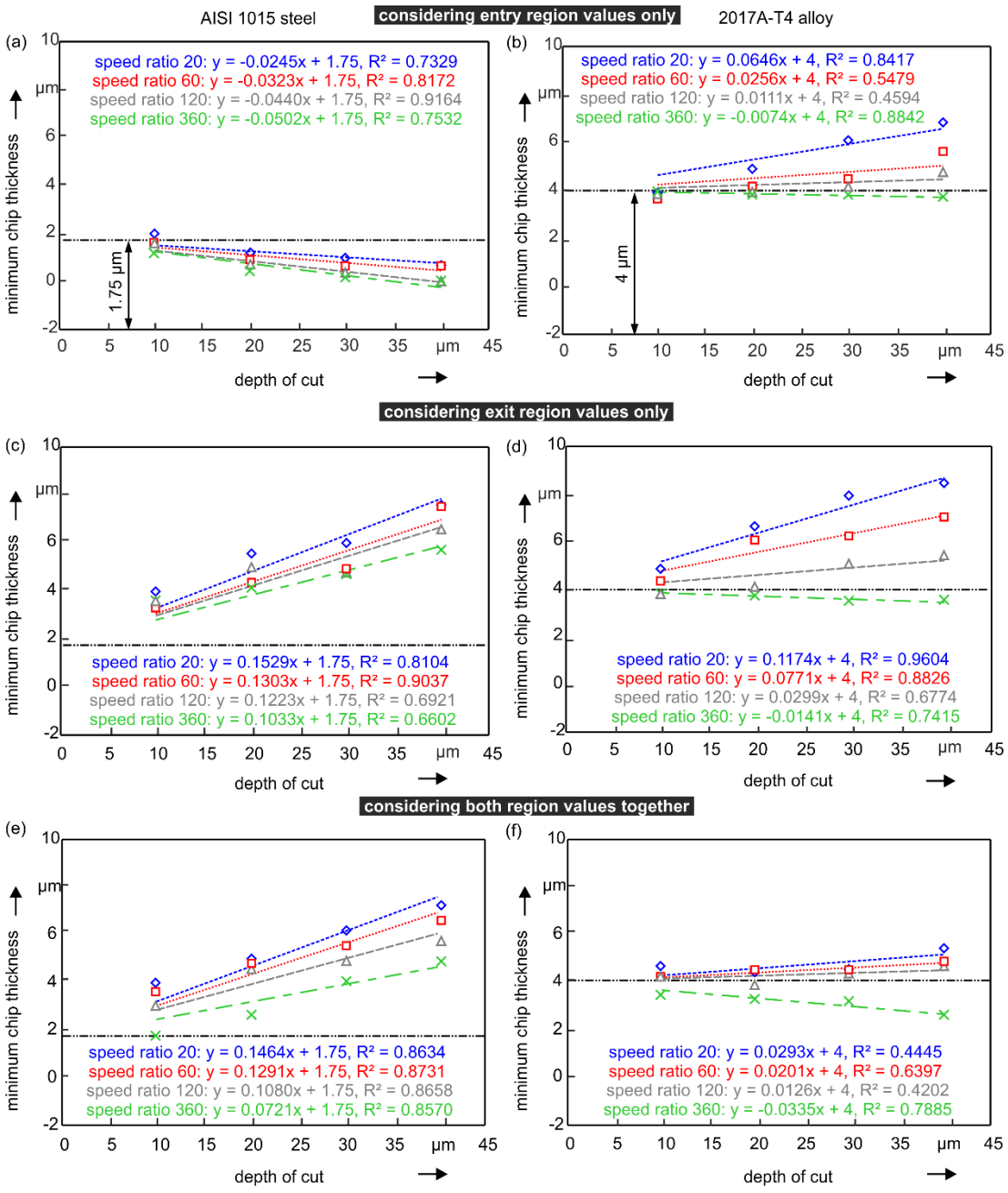

Figure 6. Variation in minimum chip thickness values for AISI 1015 steel (left) and 2017A-T4 alloy (right) considering (a, b) entry region values only (c, d) exit region values only (e, f) entry and exit region values together

From the above table 4, it can be observed that the minimum chip thickness values are not the same for any two conditions and showing a strong dependency on the set depth of cut value. It indicates that the minimum chip thickness values predicted considering only material properties and cutting edge geometry are not suitable for dynamic situations, which is evident from the percentage of error values in Table 4. Moreover, several researchers (Table 1) reported the influence of depth of cut and cutting speed on the ploughing. Hence, to further study the variation of minimum chip thickness values with kinematic conditions in the entry and exit regions, and together, figure 6 is utilised. From figures 6a – 6f, it is evident that the minimum chip thickness values are varying with the set depth of cut, speed ratio, and also on the mode of scratching (i.e., up or down).

AISI 1015 steel is showing more deviation in the exit region from the expected [45] static minimum chip thickness value (1.75 μm), unlike the entry region. Moreover, these values are higher than their static minimum chip thickness value (predicted based on the grit and work material properties and grit geometry neglecting kinematic conditions), unlike 2017A-T4 alloy. It can be attributed to the comparable thermal diffusivity of AISI 1015 steel with Si_3N_4, whereas 2017A-T4 has higher thermal diffusivity value than the Si_3N_4 and hence heat generation and the influence of temperature on the work surface is not significant. This statement also supported by Qian et al., [49] recent work. According to them, the material which had the lower thermal conductivity results in lower heat partition ratios and hence higher temperatures around the grinding zone. Accordingly, in the present work, AISI 1015 steel has lower thermal conductivity value compared to the 2017A-T4 alloy. Due to this, higher temperatures in AISI 1015 steel can be attributed to the resulted in higher minimum chip thickness values in the exit region compared to the entry region unlike 2017A-T4 alloy. Higher temperatures with the increasing depth of cut [49] can also be attributed to this increased minimum chip thickness values as shown in Figure 6. Variation in minimum chip thickness values for AISI 1015 steel (left) and 2017A-T4 alloy (right) considering (a, b) entry region values only (c, d) exit region values only (e, f) entry and exit region values together**Error! Reference source not found.**. Further, linear regression lines were drawn with an intercept equal to the static minimum chip thickness values as shown in Figure 6**Error! Reference source not found.**. Hence, the values 1.75 and 4 shown in**Error! Reference source not found.** regression equations (i.e., minimum chip thickness equations for dynamic conditions) are the predicted minimum chip thickness values under static condition for AISI 1015 steel and 2017A-T4 alloy respectively [45]. This approach similar to Malkin et al.,[50] approach for thermal analysis. Following Table 5 shows the summary of the predicted dynamic minimum chip thickness values (predicted based on the grit and work material properties, grit geometry, and kinematic conditions) using linear regression equations given in Figure 6**Error! Reference source not found.**.

*Table 5. Summary of the predicted minimum chip thickness values using linear regression equations given in Figure 6**Error! Reference source not found.**.*

S. No	a_p (μm)	q	$h_d{}'$ (μm)

			2017A-T4 alloy			AISI 1015 steel		
			$h_d'_{entry}$	$h_d'_{exit}$	$h_d'_{total}$	$h_d'_{entry}$	$h_d'_{exit}$	$h_d'_{total}$
1	10	20	4.65	5.21	4.29	1.51	3.28	3.21
2	20	20	5.29	6.42	4.59	1.26	4.81	4.68
3	30	20	5.94	7.63	4.88	1.02	6.34	6.14
4	40	20	6.58	8.84	5.17	0.77	7.87	7.61
5	10	60	4.26	4.77	4.20	1.43	3.05	3.04
6	20	60	4.51	5.54	4.40	1.10	4.36	4.33
7	30	60	4.77	6.31	4.60	0.78	5.66	5.62
8	40	60	5.02	7.08	4.80	0.46	6.96	6.91
9	10	120	4.11	4.30	4.13	1.31	2.97	2.83
10	20	120	4.22	4.60	4.25	0.87	4.20	3.91
11	30	120	4.33	4.90	4.38	0.43	5.42	4.99
12	40	120	4.44	5.20	4.50	-0.01	6.64	6.07
13	10	360	3.93	3.86	3.67	1.25	2.78	2.47
14	20	360	3.85	3.72	3.33	0.75	3.82	3.19
15	30	360	3.78	3.58	3.00	0.24	4.85	3.91
16	40	360	3.70	3.44	2.66	-0.26	5.88	4.63

Negative values in table 5 can be considered as zero as they do not have any significance. It can also be observed that on an average of 2017A-T4 alloy entry and exit region dynamic minimum chip thickness values are 1.15 and 1.34 times higher than the static minimum chip thickness value. i.e., the work material, which has higher thermal diffusivity value than the grit material has not shown much difference with its dynamic minimum chip thickness value. However, for AISI 1015 steel, entry and exit region dynamic minimum chip thickness values are 0.46 and 2.82 times higher than the static minimum chip thickness value due to the comparable thermal diffusivity value with grit material. To investigate this behaviour, an insight into the material flow with the forces and temperature is required. However, in the present work, it is not examined.

Further, using the obtained results, a methodology was developed to integrate the material pile-up behaviour in kinematic simulations. As mentioned in the introduction, the applicability of the kinematic simulation primarily depends upon the integration of accurate material removal mechanism, which includes material pile-up also. However, to the best of our knowledge, all the kinematic simulation works related to the grinding operations have not considered this phenomenon [8][9,10][12–14][15]. Hence, in this work, a methodology was developed for the single grit simulation with material pile-up. Further, it could be implemented to the multiple abrasives.

For kinematic simulations, a valid mathematical model is required to represent material pile-up, side flow, and groove geometry during the scratching. Hence, for a mathematical model, above predicted dynamic

minimum chip thickness values in each region were considered as the groove depth value at the transition position. Additionally, the following assumptions are made, which are also schematically shown in Figure 7:

i. left-side and right-side pile-up areas are the same

ii. pile-up shape considered as an acute isosceles triangle. At the transition position, it has height h_{pt} and base equal to $b/1.5$ *(based on scratch measurements shown in Figure 4a)*

iii. as mentioned earlier at the transition position (i.e. at $d = h_{d'}$) $A_1 + A_2 = A$, whereas in simulations $A = 2A_3$

iv. the material front bulging effect was not considered

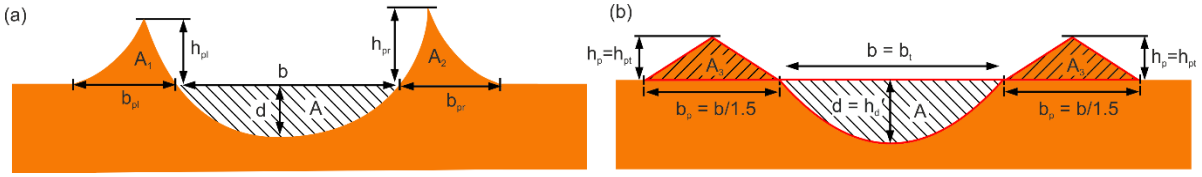

Figure 7. (a) geometrical representation of measured scratch cross-section at transition position, (b) geometrical representation of simulated scratch cross-section at the transition position

Apart from the above, other assumptions related to the kinematic simulations are also applicable such as neglecting vibrations, elastic deflections, and wear of the grit. With the known cutting edge radius (x-axis) and nose radius (z-axis) and set depth of cut (y-axis), a half-ellipsoid (grit shape for the simulations) is generated similar to the grit (cutting edge and nose radius values are 15 µm and 794 µm respectively) used in the experiments, shown in Figure 8a.

To generate an ellipsoid, following parametric equations are used:

$$x = r_o \cos u \sin v \quad (3)$$

$$z = r_e \sin u \cos v \quad (4)$$

$$y = a_p \cos v \quad (5)$$

for u ϵ [-π/2, 0] and v ϵ [-π, π]

For kinematic simulations, grit and workpiece were divided into n number of equal 2D segments along the z-axis (Figure 8b). For every slice in the XY plane, following Eq. 6 is used to simulate the scratch depth in the y-direction along the x-axis within the kinematic contact length value (Figure 8c).

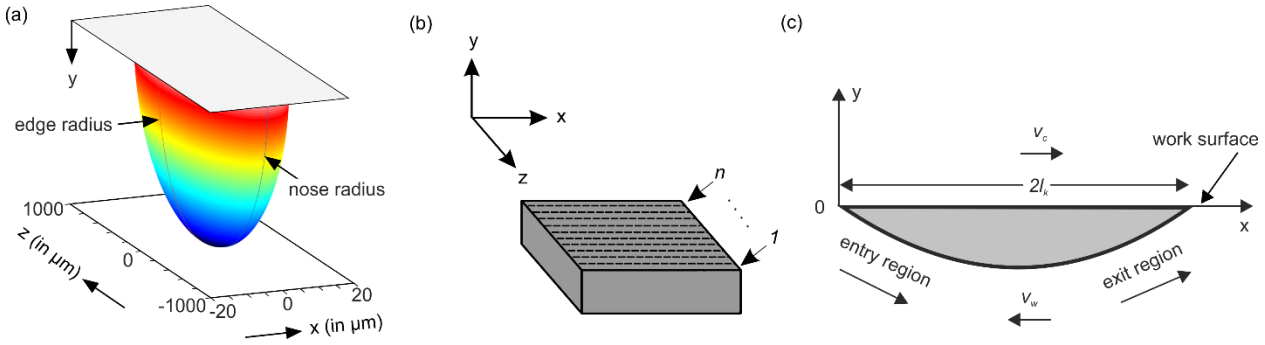

Figure 8. (a) simulated grit shape used for the kinematic simulations (b) slicing of the initial workpiece in the z-axis direction (c) system of coordinates for a single scratch in XY plane

$$y = \frac{(x-l_k)^2}{D} - a_p \qquad \text{for } 0 \le x \le l_k \tag{6}$$

Kinematic contact length (l_k) can be expressed as [51]

$$l_k = \left(1 \pm \frac{v_w}{v_c}\right)\sqrt{Da_p} \tag{7}$$

Modified 2D Z-map technique developed by Darafon [52] was used to simulate the material removal at every position of the grit in a 2D plane (XY plane). Trajectory paths of the grit cross-section in YZ plane truncated to $y = 0$ to represent the simulation without pile-up (Figure 9a). To simulate the material pile-up height, trajectory paths of the grit cross-sections in YZ plane truncated at a defined pile-up surface (power fit surface, $y = z^c$, 'c' is power fit coefficient or pile-up surface coefficient) in y-direction as shown in Figure 9b and then these values connected to the corresponding pile-up width in the z-direction.

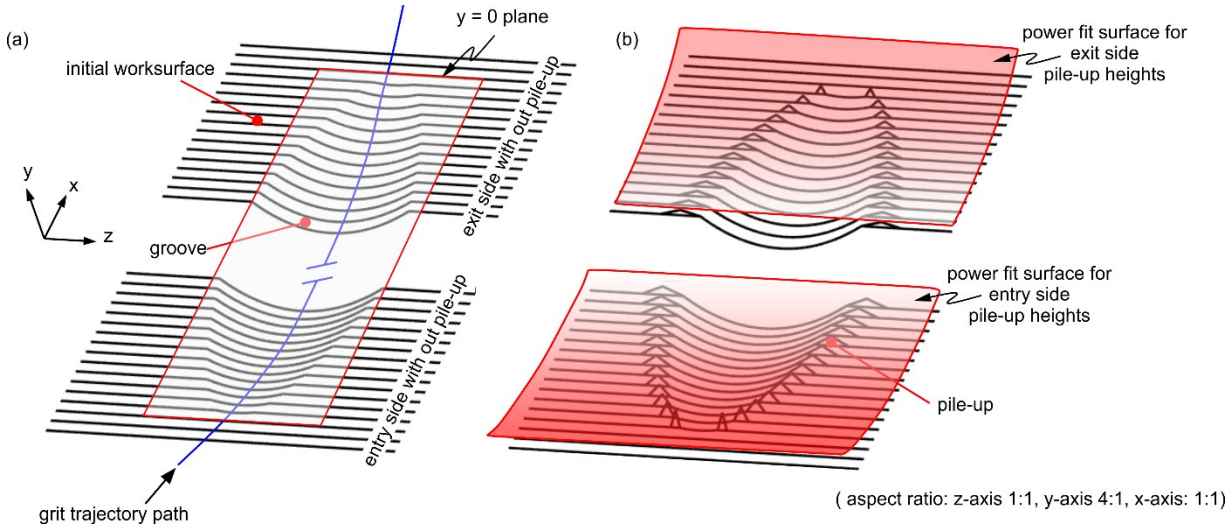

Figure 9. Schematic representation of kinematic simulation methodology (a) trajectory path of grit cross-sectional areas truncation at zero plane (b) adding up pile-up material by different power fit pile-up planes in entry and exit regions

With the known geometric relationship between the groove area and pile area at the transition position as shown in Figure 7b, pile-up surface coefficient value can be calculated. Because, to estimate the pile-up height at every position corresponding to known pile-up width value, pile-up surface coefficient value is necessary. The shape of the scratch is defined by the grit's maximum cross-sectional area projected in the YZ plane. In this case, due to the symmetry about $x = 0$, grit's maximum cross-sectional area is equal to the tool nose radius profile (Figure 8a). Profile of the grit's maximum cross-sectional area in the YZ plane at $x = 0$ can be represented as the circle with the defined edge radius (r_e)value as given below:

$$y^2 + z^2 = r_e^2 \tag{8}$$

Scratch width (or groove width) corresponding to the depth can be calculated with the following equation:

$$b = 2\sqrt{d(2r_e - d)} \tag{9}$$

If b_t is the width of the scratch at the transition position (or at the minimum chip thickness value(h'_d), it can be calculated with the following equation:

$$b_t = 2\sqrt{h'_d(2r_e - h'_d)} \tag{10}$$

by considering the relation between the pile-up area and groove area at the transition position (based on Figure 7b), pile-up height (h_{pt}) can be calculated by solving the equation 11.

$A = 2A_3$

$$r_e{}^2 \cos^{-1}\left(\frac{r_e - h'_d}{r_e}\right) - (r_e - h'_d)\sqrt{2r_e h'_d - h'_d{}^2} = \frac{bh_{pt}}{3} \tag{11}$$

Substituting the values of b (equation 9), and other known variables (r_e and h'_d(Table 5)) in the above Eq. 11 results in h_{pt} value. Summary of the predicted pile-up height values using equation 11, at the transition position are given in Table 6.

Table 6. Summary of the predicted pile-up height values at the transition position

S. No	a_p (µm)	q	h_{pt} (µm)					
			2017A-T4 alloy			AISI 1015 steel		
			h'_{entry}	h'_{exit}	h'_{total}	h'_{entry}	h'_{exit}	h'_{total}
1	10	20	4.65	5.21	4.32	1.51	3.28	3.11
2	20	20	5.29	6.42	4.64	1.26	4.81	4.47
3	30	20	5.94	7.63	4.96	1.02	6.34	5.83
4	40	20	6.58	8.84	5.28	0.77	7.87	7.19
5	10	60	4.26	4.77	4.24	1.43	3.05	3.03
6	20	60	4.51	5.54	4.48	1.10	4.36	4.31
7	30	60	4.77	6.31	4.72	0.78	5.66	5.59
8	40	60	5.02	7.08	4.96	0.46	6.96	6.87

9	10	120	4.11	4.30	4.12	1.31	2.97	2.91
10	20	120	4.22	4.60	4.24	0.87	4.20	4.07
11	30	120	4.33	4.90	4.36	0.43	5.42	5.23
12	40	120	4.44	5.20	4.48	0	6.64	6.39
13	10	360	3.93	3.86	3.64	1.25	2.78	2.43
14	20	360	3.85	3.72	3.28	0.75	3.82	3.11
15	30	360	3.78	3.58	2.92	0.24	4.85	3.79
16	40	360	3.70	3.44	2.56	0	5.88	4.47

After knowing the h_{pt} value at the transition position, it is possible to estimate the power fit surface coefficient 'c' using equation 14.

$$y = z^c \tag{12}$$

$$c = \frac{log\, y}{log\, z} \tag{13}$$

where 'y' is the pile-up height (h_{pt}) and 'z' is the pile-up width (b_t) at the transition position.

$$c = \frac{log\, h_{pt}}{log(b_t)} \tag{14}$$

Now at every position, corresponding to the pile-up width value, pile-up height can be calculated using the 'c' value as given below:

$$h_p = {b_p}^c \tag{15}$$

$$h_p = b_p^{\frac{log\, h_{pt}}{log(b_t)}} \tag{16}$$

where b_p is the pile-up width, which is equal to $b/1.5$ as per assumptions (Figure 7b and Figure 4a).
With the help of the developed method, kinematic simulations were done for a length of $2l_k$. **Error! Reference source not found.** Figure 10 shows the simulated scratch surfaces for the studied materials at the same speed ratio and depth of cut.

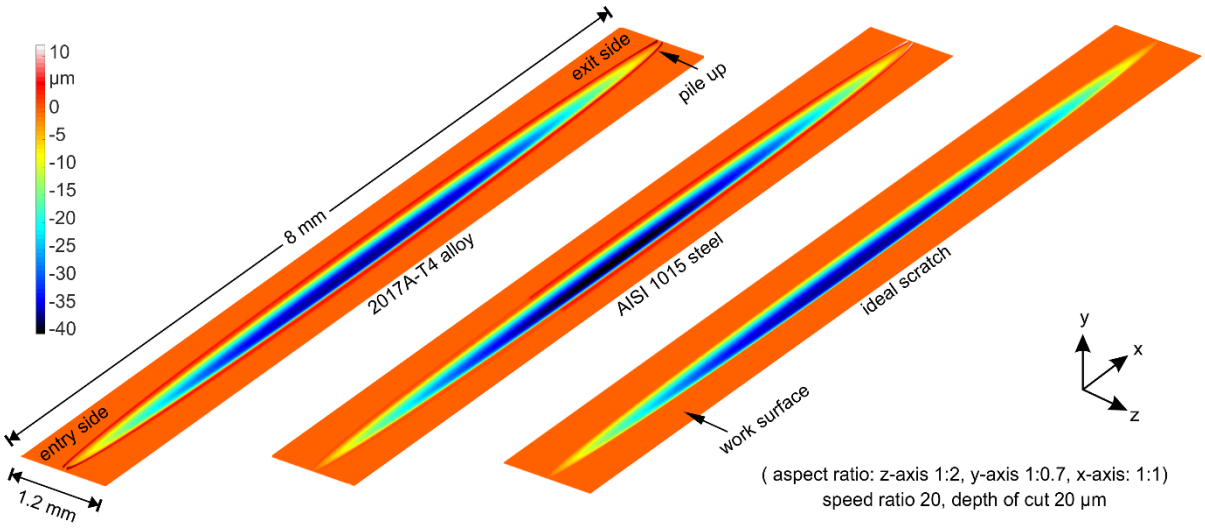

Figure 10. Simulated scratch surfaces showing the material dependent pile-up behaviour

Further, to show the variations with the kinematic conditions, simulations were done for the entry and exit sides separately and shown in Figure 11 and Figure 12, also compared with the scratch surfaces resulted from the experiments. It can be observed that the pile-up behaviour is decreasing with the increasing speed ratio like the minimum chip thickness variation (Figure 6**Error! Reference source not found.**). Figure 12 shows the exit sides of the simulated scratch surfaces variation with depth of cut. It can also be observed that at the entry side, the pile-up behaviour is decreasing at a higher depth of cuts with the increasing speed ratio. Developed simulation method also shows the variations in line with the several other researcher's observations (Table 1) and with the current experimental findings.

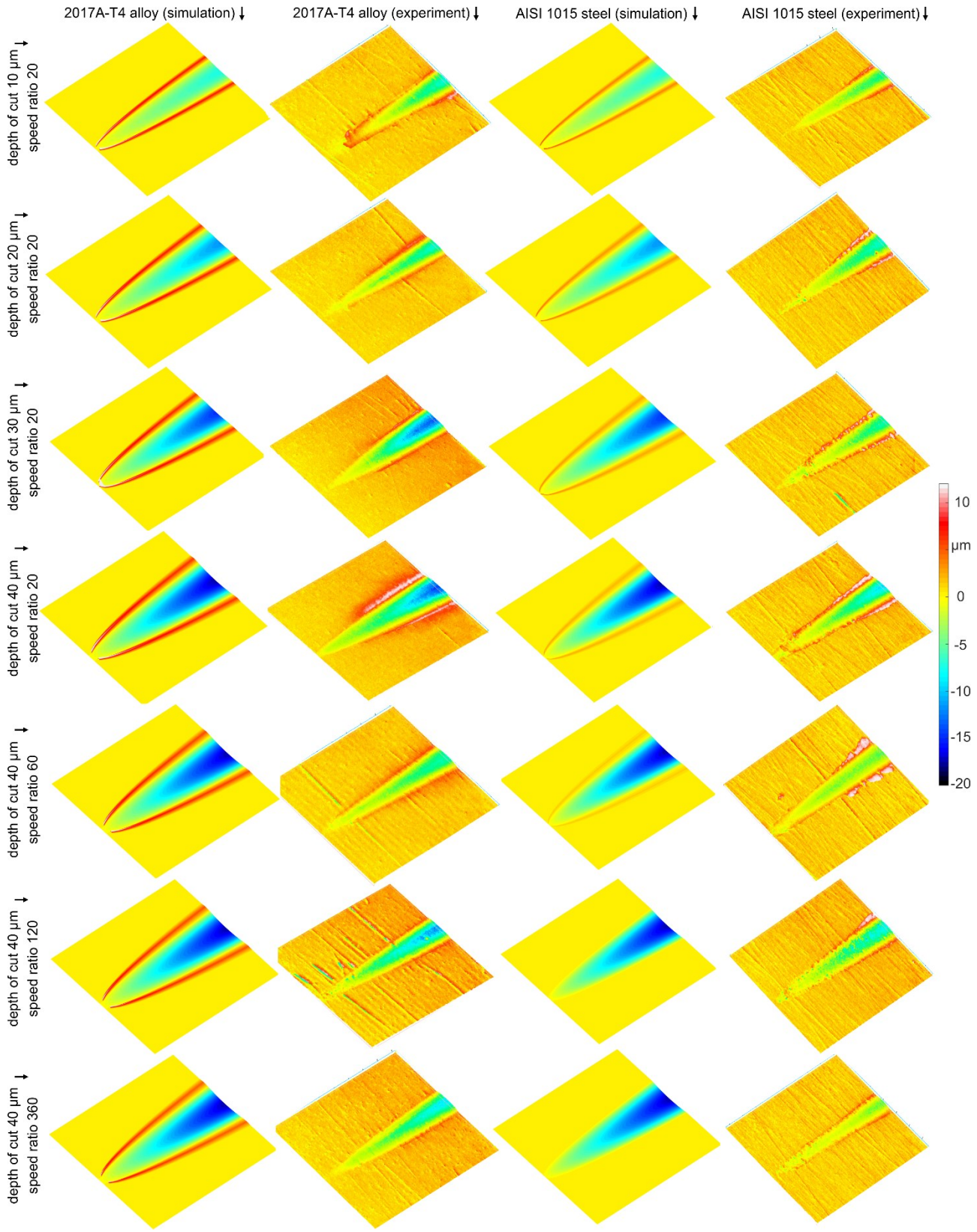

Figure 11. Scratch surface variations at the entry side with speed ratio and depth of cut

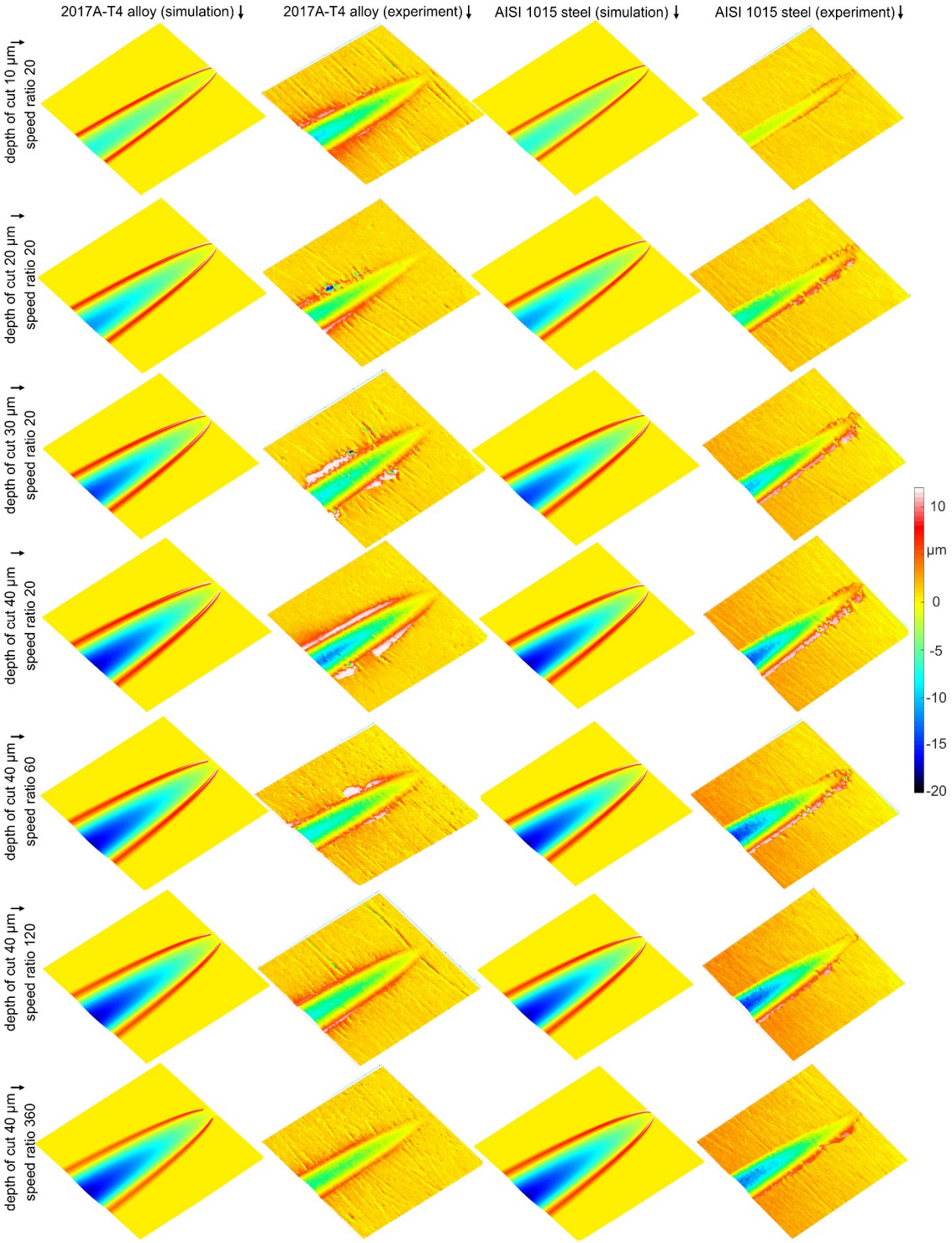

Figure 12. Scratch surface variations at the exit side with speed ratio and depth of cut

From the above experimental and simulation results, it can be observed that simulation results are able to represent the groove shape varies according to the experimental results. However, from the experimental results, it can be seen from the entry side groove depth values that AISI 1015 steel has not shown variations according to the depth of cut, which can be attributed to the initial grit and workpiece contact deflections resulted from AISI 1015 steel higher yield strength value compared to 2017A-T4 alloy [53]. As the deflection issues were not considered in the model and the same not reflected in simulations.

Conclusion and Outlook: In the present work, with the help of several single grit scratch test results on AISI 1015 steel and 2017A-T4 aluminium alloy materials, kinematic simulations were done considering predicted dynamic minimum chip thickness values where the transition from ploughing to cutting occurs. These simulations included material pile-up because of ploughing.

With the help of experimental results on AISI 1015 steel and 2017A-T4 aluminium alloy work materials, the following conclusions were drawn:

i. minimum chip thickness value was dependent on the grit and work material combinations as well as kinematic conditions.
ii. with an increase in the depth of cut, minimum chip thickness value in the exit region increases for both the materials and deviates significantly from their static minimum chip thickness values at lower speed ratios.
iii. AISI 1015 steel, which has comparable thermal diffusivity with the Si_3N_4 grit has shown significant differences in between the entry and, exit region minimum chip thickness values. Whereas,2017A-T4 alloy has higher thermal diffusivity than the Si_3N_4 grit and not shown significant differences with chip thickness variation.
iv. decreasing ploughing behaviour at higher speed ratios can be attributed to the effective thermal diffusivity ratio of grit and work material. i.e., 2017A-T4 alloy, which has higher thermal diffusivity value than the Si_3N_4 grit showed more ploughing behaviour than the AISI 1015 steel.
v. proposed simulation technique with single grit considering the pile-up behaviour can be expanded to multiple abrasive grits interaction.

Acknowledgment: 'Funded by the Deutsche Forschungsgemeinschaft (DFG, German Research Foundation) – 252408385 – IRTG 2057'

References:

[1] F. Hashimoto, H. Yamaguchi, P. Krajnik, K. Wegener, R. Chaudhari, H.-W. Hoffmeister, F. Kuster, Abrasive fine-finishing technology, CIRP Annals 65 (2016) 597–620. https://doi.org/10.1016/j.cirp.2016.06.003.

[2] J.F.G. Oliveira, E.J. Silva, C. Guo, F. Hashimoto, Industrial challenges in grinding, CIRP Annals 58 (2009) 663–680. https://doi.org/10.1016/j.cirp.2009.09.006.

[3] E. Brinksmeier, J.C. Aurich, E. Govekar, C. Heinzel, H.-W. Hoffmeister, F. Klocke, J. Peters, R. Rentsch, D.J. Stephenson, E. Uhlmann, K. Weinert, M. Wittmann, Advances in Modeling and Simulation of Grinding Processes, CIRP Annals 55 (2006) 667–696. https://doi.org/10.1016/j.cirp.2006.10.003.

[4] M.P. Lautenschlaeger, S. Stephan, H.M. Urbassek, B. Kirsch, J.C. Aurich, M.T. Horsch, H. Hasse, Effects of Lubrication on the Friction in Nanometric Machining Processes: A Molecular Dynamics Approach, AMM 869 (2017) 85–93. https://doi.org/10.4028/www.scientific.net/AMM.869.85.

[5] D.A. Doman, A. Warkentin, R. Bauer, Finite element modeling approaches in grinding, International Journal of Machine Tools and Manufacture 49 (2009) 109–116. https://doi.org/10.1016/j.ijmachtools.2008.10.002.

[6] C. Su, X. Mi, X. Sun, M. Chu, Simulation study on chip formation mechanism in grinding particle reinforced Cu-matrix composites, The International Journal of Advanced Manufacturing Technology 99 (2018) 1249–1256. https://doi.org/10.1007/s00170-018-2477-9.

[7] H.-Q. Chen, Q.-H. Wang, A novel approach to simulate surface topography based on motion trajectories and feature theories of abrasive grains, The International Journal of Advanced Manufacturing Technology 99 (2018) 1467–1480. https://doi.org/10.1007/s00170-018-2590-9.

[8] J.C. Aurich, B. Kirsch, Kinematic simulation of high-performance grinding for analysis of chip parameters of single grains, CIRP Journal of Manufacturing Science and Technology 5 (2012) 164–174. https://doi.org/10.1016/j.cirpj.2012.07.004.

[9] Y. Cao, J. Guan, B. Li, X. Chen, J. Yang, C. Gan, Modeling and simulation of grinding surface topography considering wheel vibration, The International Journal of Advanced Manufacturing Technology 66 (2013) 937–945. https://doi.org/10.1007/s00170-012-4378-7.

[10] X. Wang, T. Yu, Y. Dai, Y. Shi, W. Wang, Kinematics modeling and simulating of grinding surface topography considering machining parameters and vibration characteristics, The International Journal of Advanced Manufacturing Technology 87 (2016) 2459–2470. https://doi.org/10.1007/s00170-016-8660-y.

[11] X. Chen, W.B. Rowe, B. Mills, D.R. Allanson, Analysis and simulation of the grinding process. Part IV: Effects of wheel wear, International Journal of Machine Tools and Manufacture 38 (1998) 41–49. https://doi.org/10.1016/S0890-6955(97)00041-2.

[12] Y. Liu, A. Warkentin, R. Bauer, Y. Gong, Investigation of different grain shapes and dressing to predict surface roughness in grinding using kinematic simulations, Precision Engineering 37 (2013) 758–764. https://doi.org/10.1016/j.precisioneng.2013.02.009.

[13] H. Chen, T. Yu, J. Dong, Y. Zhao, J. Zhao, Kinematic simulation of surface grinding process with random cBN grain model, The International Journal of Advanced Manufacturing Technology (2018). https://doi.org/10.1007/s00170-018-2840-x.

[14] H. Yu, J. Wang, Y. Lu, Simulation of grinding surface roughness using the grinding wheel with an abrasive phyllotactic pattern, The International Journal of Advanced Manufacturing Technology 84 (2016) 861–871. https://doi.org/10.1007/s00170-015-7722-x.

[15] J.L. Jiang, P.Q. Ge, W.B. Bi, L. Zhang, D.X. Wang, Y. Zhang, 2D/3D ground surface topography modeling considering dressing and wear effects in grinding process, International Journal of Machine Tools and Manufacture 74 (2013) 29–40. https://doi.org/10.1016/j.ijmachtools.2013.07.002.

[16] E. Uhlmann, S. Koprowski, W.L. Weingaertner, D.A. Rolon, Modelling and Simulation of Grinding Processes with Mounted Points: Part II of II - Fast Modelling Method for Workpiece Surface Prediction, Procedia CIRP 46 (2016) 603–606. https://doi.org/10.1016/j.procir.2016.03.202.

[17] A. McDonald, A.-M.O. Mohamed, A. Warkentin, R.J. Bauer, Kinematic simulation of the uncut chip thickness and surface finish using a reduced set of 3D grinding wheel measurements, Precision Engineering 49 (2017) 169–178. https://doi.org/10.1016/j.precisioneng.2017.02.005.

[18] I. Inasaki, Grinding Process Simulation Based on the Wheel Topography Measurement, CIRP Annals 45 (1996) 347–350. https://doi.org/10.1016/S0007-8506(07)63077-7.

[19] J.C. Aurich, O. Braun, G. Warnecke, L. Cronjäger, Development of a Superabrasive Grinding Wheel With Defined Grain Structure Using Kinematic Simulation, CIRP Annals 52 (2003) 275–280. https://doi.org/10.1016/S0007-8506(07)60583-6.

[20] J. Chi, J. Guo, L. Chen, The study on a simulation model of workpiece surface topography in external cylindrical grinding, The International Journal of Advanced Manufacturing Technology 82 (2016) 939–950. https://doi.org/10.1007/s00170-015-7406-6.

[21] S. Malkin, C. Guo, Grinding technology: Theory and application of machining with abrasives, Industrial Press, New York, 2008.

[22] M.E.A. Moneim, A.A. Nasser, A.M.A. Mahboud, Reciprocation of negative rake edges to simulate grinding with zero nominal depth of cut, Wear 84 (1983) 81–85. https://doi.org/10.1016/0043-1648(83)90120-5.

[23] D. Graham, R.M. Baul, An investigation into the mode of metal removal in the grinding process, Wear 19 (1972) 301–314. https://doi.org/10.1016/0043-1648(72)90122-6.

[24] W.B. Rowe, X. Chen, Characterization of the size effect in grinding and the sliced bread analogy, International Journal of Production Research 35 (1997) 887–899. https://doi.org/10.1080/002075497195768.

[25] K. Cheng, D. Huo, Micro-cutting: Fundamentals and applications / editors: Kai Cheng, Brunel University, UK, Dehong Huo, Newcastle University, UK, Wiley, Chichester, West Sussex, United Kingdom, 2013.

[26] T.T. Öpöz, Investigation of Material Removal Mechanism in Grinding: A Single Grit Approach. PhD, Huddersfield, 2012.

[27] T.C. Buttery, M.S. Hamed, Some factors affecting the efficiency of individual grits in simulated grinding experiments, Wear 44 (1977) 231–245. https://doi.org/10.1016/0043-1648(77)90142-9.

[28] T.C. Buttery, M.S. Hamed, The Generation of Random Surfaces Representative of Abrasion, Journal of Mechanical Engineering Science 20 (1978) 133–141. https://doi.org/10.1243/JMES_JOUR_1978_020_024_02.

[29] Y. Kita, M. Ido, Y. Tuji, The influence of the cutting speed on the mechanism of metal removal by an abrasive tool, Wear 71 (1981) 55–63. https://doi.org/10.1016/0043-1648(81)90139-3.

[30] T. Matsuo, S. Toyoura, E. Oshima, Y. Ohbuchi, Effect of Grain Shape on Cutting Force in Superabrasive Single-Grit Tests, CIRP Annals 38 (1989) 323–326. https://doi.org/10.1016/S0007-8506(07)62714-0.

[31] Y. Ohbuchi, T. Matsuo, Force and Chip Formation in Single-Grit Orthogonal Cutting with Shaped CBN and Diamond Grains, CIRP Annals 40 (1991) 327–330. https://doi.org/10.1016/S0007-8506(07)61998-2.

[32] H. Wang, G. Subhash, A. Chandra, Characteristics of single-grit rotating scratch with a conical tool on pure titanium, Wear 249 (2001) 566–581. https://doi.org/10.1016/S0043-1648(01)00585-3.

[33] F. Klocke, T. Beck, S. Hoppe, T. Krieg, N. Müller, T. Nöthe, H.-W. Raedt, K. Sweeney, Examples of FEM application in manufacturing technology, Journal of Materials Processing Technology 120 (2002) 450–457. https://doi.org/10.1016/S0924-0136(01)01210-9.

[34] G. Subhash, W. Zhang, Investigation of the overall friction coefficient in single-pass scratch test, Wear 252 (2002) 123–134. https://doi.org/10.1016/S0043-1648(01)00852-3.

[35] E. Brinksmeler, A. Glwerzew, Chip Formation Mechanisms in Grinding at Low Speeds, CIRP Annals 52 (2003) 253–258. https://doi.org/10.1016/S0007-8506(07)60578-2.

[36] M. Barge, J. Rech, H. Hamdi, J.-M. Bergheau, Experimental study of abrasive process, Wear 264 (2008) 382–388. https://doi.org/10.1016/j.wear.2006.08.046.

[37] S. Ghosh, A.B. Chattopadhyay, S. Paul, Study of grinding mechanics by single grit grinding test, International Journal of Precision Technology 1 (2010) 356. https://doi.org/10.1504/IJPTECH.2010.031663.

[38] J.C. Aurich, M. Steffes, Single Grain Scratch Tests to Determine Elastic and Plastic Material Behavior in Grinding, Advanced Materials Research 325 (2011) 48–53. https://doi.org/10.4028/www.scientific.net/AMR.325.48.

[39] D. Anderson, A. Warkentin, R. Bauer, Experimental and numerical investigations of single abrasive-grain cutting, International Journal of Machine Tools and Manufacture 51 (2011) 898–910. https://doi.org/10.1016/j.ijmachtools.2011.08.006.

[40] T.T. Öpöz, X. Chen, Experimental investigation of material removal mechanism in single grit grinding, International Journal of Machine Tools and Manufacture 63 (2012) 32–40. https://doi.org/10.1016/j.ijmachtools.2012.07.010.

[41] C.-W. Dai, T.-Y. Yu, W.-F. Ding, J.-H. Xu, Z. Yin, H. Li, Single diamond grain cutting-edges morphology effect on grinding mechanism of Inconel 718, Precision Engineering 55 (2019) 119–126. https://doi.org/10.1016/j.precisioneng.2018.08.017.

[42] L. Tian, Y. Fu, J. Xu, H. Li, W. Ding, The influence of speed on material removal mechanism in high speed grinding with single grit, International Journal of Machine Tools and Manufacture 89 (2015) 192–201. https://doi.org/10.1016/j.ijmachtools.2014.11.010.

[43] J.G. Wager, D.Y. Gu, Influence of Up-Grinding and Down-Grinding on the Contact Zone, CIRP Annals 40 (1991) 323–326. https://doi.org/10.1016/S0007-8506(07)61997-0.

[44] S.-B. Wang, H.-S. Kou, Selections of working conditions for creep feed grinding. Part(II): workpiece temperature and critical grinding energy for burning, The International Journal of Advanced Manufacturing Technology 28 (2006) 38–44. https://doi.org/10.1007/s00170-004-2344-8.

[45] D. Setti, B. Kirsch, J.C. Aurich, An Analytical Method for Prediction of Material Deformation Behavior in Grinding Using Single Grit Analogy, Procedia CIRP 58 (2017) 263–268. https://doi.org/10.1016/j.procir.2017.03.193.

[46] W.B. Rowe (Ed.), Principles of modern grinding technology, William Andrew, Amsterdam, 2014.

[47] http://www.matweb.com (accessed 2 January 2018).

[48] C. Gauthier, R. Schirrer, Time and temperature dependence of the scratch properties of poly(methylmethacrylate) surfaces, Journal of Materials Science 35 (2000) 2121–2130. https://doi.org/10.1023/A:1004798019914.

[49] N. Qian, W. Ding, Y. Zhu, Comparative investigation on grindability of K4125 and Inconel718 nickel-based superalloys, The International Journal of Advanced Manufacturing Technology 97 (2018) 1649–1661. https://doi.org/10.1007/s00170-018-1993-y.

[50] S. Malkin, C. Guo, Thermal Analysis of Grinding, CIRP Annals 56 (2007) 760–782. https://doi.org/10.1016/j.cirp.2007.10.005.

[51] O.E. Saljé, R. Paulmann, Relations Between Abrasive Processes, CIRP Annals 37 (1988) 641–648. https://doi.org/10.1016/S0007-8506(07)60761-6.

[52] A. Darafon, Measuring and Modeling of Grinding Wheel Topography. Ph.D, Halifax, Nova Scotia, 2013.

[53] D.P. Saini, A New Model of Local Elastic Deflections in Grinding, J. Vib. Acoust. 106 (1984) 154. https://doi.org/10.1115/1.3269144.